Radar imaging and physical characterization of near-Earth Asteroid (162421) 2000 ET70

Shantanu P. Naidu [a,*], Jean-Luc Margot [a,b], Michael W. Busch [a,1], Patrick A. Taylor [c], Michael C. Nolan [c], Marina Brozovic [d], Lance A.M. Benner [d], Jon D. Giorgini [d], Christopher Magri [e]

[a] Department of Earth and Space Sciences, University of California, Los Angeles, 595 Charles Young Drive East, Los Angeles, CA 90095, USA
[b] Department of Physics and Astronomy, University of California, Los Angeles, 430 Portola Plaza, Los Angeles, CA 90095, USA
[c] Arecibo Observatory, HC3 Box 53995, Arecibo, PR 00612, USA
[d] Jet Propulsion Laboratory, California Institute of Technology, Pasadena, CA 91109-8099, USA
[e] University of Maine at Farmington, 173 High Street, Preble Hall, Farmington, ME 04938, USA

ARTICLE INFO

ABSTRACT

We observed near-Earth Asteroid (162421) 2000 ET70 using the Arecibo and Goldstone radar systems over a period of 12 days during its close approach to the Earth in February 2012. We obtained continuous wave spectra and range-Doppler images with range resolutions as fine as 15 m. Inversion of the radar images yields a detailed shape model with an effective spatial resolution of 100 m. The asteroid has overall dimensions of 2.6 km × 2.2 km × 2.1 km (5% uncertainties) and a surface rich with kilometer-scale ridges and concavities. This size, combined with absolute magnitude measurements, implies an extremely low albedo (∼2%). It is a principal axis rotator and spins in a retrograde manner with a sidereal spin period of 8.96 ± 0.01 h. In terms of gravitational slopes evaluated at scales of 100 m, the surface seems mostly relaxed with over 99% of the surface having slopes less than 30°, but there are some outcrops at the north pole that may have steeper slopes. Our precise measurements of the range and velocity of the asteroid, combined with optical astrometry, enables reliable trajectory predictions for this potentially hazardous asteroid in the interval 460–2813.

1. Introduction

Radar astronomy is arguably the most powerful Earth-based technique for characterizing the physical properties of near-Earth asteroids (NEAs). Radar observations routinely provide images with decameter spatial resolution. These images can be used to obtain accurate astrometry, model shapes, measure near-surface radar scattering properties, and investigate many other physical properties (e.g. sizes, spin states, masses, densities). Radar observations have led to the discovery of asteroids exhibiting non-principal axis rotation (e.g., Ostro et al., 1995; Benner et al., 2002), binary and triple NEAs (e.g., Margot et al., 2002; Ostro et al., 2006; Shepard et al., 2006; Nolan et al., 2008; Brozović et al., 2011), and contact binary asteroids (e.g., Hudson and Ostro, 1994; Benner et al., 2006; Brozovic et al., 2010). Radar-derived shapes and spins have been used to investigate various physical processes (Yarkovsky, YORP, BYORP, tides, librations, precession, etc.) that are important to the evolution of NEAs (e.g., Chesley et al., 2003; Nugent et al., 2012; Lowry et al., 2007; Taylor et al., 2007; Ostro et al., 2006; Scheeres et al., 2006; Taylor and Margot, 2011; Fang et al., 2011; Fang and Margot, 2012).

Here we present the radar observations and detailed physical characterization of NEA (162421) 2000 ET70. This Aten asteroid (a = 0.947 AU, e = 0.124, i = 22.3°) was discovered on March 8, 2000 by the Lincoln Near-Earth Asteroid Research (LINEAR) program in Socorro, New Mexico. Its absolute magnitude was reported to be 18.2 (Whiteley, 2001) which, for typical optical albedos between 0.4 and 0.04, suggests a diameter between 0.5 and 1.5 km. Recent analysis of the astrophotometry yields absolute magnitude values that are comparable (Williams, 2012). Alvarez et al. (2012) obtained a lightcurve of the asteroid during its close approach to the Earth in February 2012. They reported a lightcurve period of 8.947 ± 0.001 h and a lightcurve amplitude of 0.60 ± 0.07. Using visible photometry, Whiteley (2001) classified 2000 ET70 as an X-type asteroid in the Tholen (1984) taxonomy. The Tholen X class is a degenerate group of asteroids consisting of E, M, and P classes, which are distinguished by albedo. Mike Hicks (personal communication) used visible spectroscopy and indicated that his observations best matched a C-type or possibly an E-type. Using spectral observations covering a wavelength range of 0.8–2.5 μm in addition to the visible data, Ellen Howell (personal communication) classified it as Xk in the taxonomic system of Bus-DeMeo (DeMeo et al., 2009).

* Corresponding author. Address: Department of Earth and Space Sciences, University of California, Los Angeles, 595 Charles Young Drive East, 5656 Geology Building, Los Angeles, CA90095, USA.
E-mail address: spn@ucla.edu (S.P. Naidu).
[1] Present address: National Radio Astronomy Observatory, 1003 Lopezville Road, Socorro, NM 87801, USA.

2. Observations and data processing

We observed 2000 ET70 from February 12, 2012 to February 17, 2012 using the Arecibo S-band (2380 MHz, 13 cm) radar and from February 15, 2012 to February 23, 2012 using the Goldstone X-band (8560 MHz, 3.5 cm) radar. The asteroid moved ~74 degrees across the sky during this time and it came closest to Earth on February 19 at a distance of ~0.045 Astronomical Units (AU). We observed it again in August 2012 when it made another close approach to Earth at a distance of ~0.15 AU.

Radar observing involved transmitting a radio wave for approximately the round-trip light-time (RTT) to the asteroid, ~46 s at closest approach, and then receiving the echo reflected back from the target for a comparable duration. Each transmit-receive cycle is called a *run*. On each day we carried out runs with a monochromatic continuous wave (CW) to obtain Doppler spectra, followed by runs with a modulated carrier to obtain range-Doppler images. CW data are typically used to measure total echo power and frequency extent, whereas range-Doppler images are typically used to resolve the target in two dimensions. Table 1 summarizes the CW and range-Doppler imaging runs.

For CW runs a carrier wave at a fixed frequency was transmitted for the RTT to the asteroid. The received echo from the asteroid was demodulated, sampled, and recorded. A fast Fourier transform (FFT) was applied to each echo timeseries to obtain the CW spectra. The total frequency extent (Δf) or bandwidth (BW) of the CW spectra is equal to the sampling frequency (f_s) or the reciprocal of the sampling period (P_s):

$$\Delta f = f_s = \frac{1}{P_s}. \tag{1}$$

The spectral resolution (δf) is given by:

$$\delta f = \frac{\Delta f}{n}, \tag{2}$$

where n is the FFT length. Finer spectral resolution can be achieved by increasing n, however the signal-to-noise ratio (SNR) in each frequency bin decreases as $1/\sqrt{n}$. The finest possible resolution that can be achieved is limited by the number of samples obtained in one run. If we were recording for the full duration of the RTT, the number of samples obtained in one run would be $n = \text{RTT} \times f_s$, and the resolution would be $\delta f = 1/\text{RTT}$. In reality we cannot transmit for a full RTT as it takes several seconds to switch between transmission and reception, so the finest possible resolution is $\delta f = 1/(\text{RTT} - t_{\text{switch}})$, where t_{switch} is the switching time.

For range-Doppler imaging two different *pulse compression* techniques were used to achieve fine range resolution while maintaining adequate SNR (Peebles, 2007). Pulse compression is a signal conditioning and processing technique used in radar systems to achieve a high range resolution without severely compromising the ability to detect or image the target. The range resolution achievable by a radar is proportional to the pulse duration, or, equivalently, inversely proportional to the effective bandwidth of the transmitted signal. However, decreasing the pulse duration reduces the total transmitted energy per pulse and hence it negatively affects the ability to detect the radar target. Pulse compression techniques allow for the transmission of a long pulse while still achieving the resolution of a short pulse.

2.1. Pulse compression using binary phase coding (BPC)

We used binary codes to produce range-Doppler images of the asteroid at both Arecibo and Goldstone. In this technique we modulated the transmitted carrier with a repeating pseudo-random code using binary phase shift keying (BPSK). The code contains N elements or *bauds* and the duration of each baud is T_{baud}. The duration of the code is called the pulse repetition period (PRP = $N \times T_{\text{baud}}$). The effective bandwidth of the transmitted signal (B_{eff}) is given by $1/T_{\text{baud}}$. For

each run we transmitted for approximately the RTT to the asteroid, followed by reception for a similar duration. The received signal was demodulated and then decoded by cross-correlating it with a replica of the transmitted code. The images span a range (Δr) given by:

$$\Delta r = \frac{c}{2} \text{PRP}, \tag{3}$$

and their range resolution (δr) is given by:

$$\delta r = \frac{c}{2} T_{\text{baud}} = \frac{c}{2} \frac{1}{B_{\text{eff}}}, \tag{4}$$

where c is the speed of light. Each baud within the code eventually maps into a particular range bin in the image. Resolution in the frequency or Doppler dimension was obtained in each range bin by performing a FFT on the sequence of returns corresponding to that bin. The total frequency extent (Δf) or bandwidth (BW) of the image is equal to the pulse repetition frequency (PRF) or the reciprocal of the PRP:

$$\Delta f = \text{PRF} = \frac{1}{\text{PRP}}. \tag{5}$$

The frequency resolution (δf) of the image depends on the FFT length (n) as follows:

$$\delta f = \frac{\Delta f}{n}. \tag{6}$$

The RTT dictates the finest frequency resolution achievable, similar to the situation with CW spectra.

2.2. Pulse compression using linear frequency modulation (Chirp)

We also used a linear frequency modulation technique (Margot, 2001; Peebles, 2007) to produce range-Doppler images of the asteroid at Goldstone. Only a fraction of the images were obtained in this mode because this new capability is still in the commissioning phase. Chirp waveforms allow us to maximize the bandwidth of the transmitted signal and to obtain better range resolution than that available with BPC waveforms. They are also less susceptible to degradation due to the Doppler spread of the targets. Finally, they are more amenable to the application of windowing functions that can be used to trade between range resolution and range sidelobe level (Margot, 2001).

In this technique the carrier was frequency modulated with a linear ramp signal. The resultant signal had a frequency that varied linearly with time from $\omega_0 - \omega$ to $\omega_0 + \omega$, where ω_0 is the carrier frequency and $B_{\text{eff}} = 2\omega$ is the effective bandwidth of the signal. The resultant signal is called a chirp. A repeating chirp was transmitted with 100% duty cycle for the duration of the round-trip light-time to the asteroid. The time interval between the transmission of two consecutive chirps is the PRP. For our observations we used PRPs of 125 μs and 50 μs for chirps with $B_{\text{eff}} = 2$ MHz and $B_{\text{eff}} = 5$ MHz, respectively. The received signal was demodulated and range compression was achieved by cross-correlating the echo with a replica of the transmitted signal. The range extent and the range resolution of the chirp images are given by Eqs. (3) and (4), respectively. Resolution in the frequency or Doppler dimension was obtained as in the binary coding technique. The bandwidth of the image is given by Eq. (5) and the frequency resolution is given by Eq. (6).

3. Astrometry and orbit

A radar astrometric measurement consists of a range or Doppler estimate of hypothetical echoes from the center of mass (COM) of the object at a specified coordinated universal time (UTC). In practice we used our measurements of the position of the leading edge of the echoes and our estimates of the object's size to report preliminary COM range estimates and uncertainties. We refined those estimates after we obtained a detailed shape model (Section 7). We measured Doppler astrometry from the CW spectra. We reported 9 range estimates and 1 Doppler estimate during the

Table 1
2000 ET70 radar observations log.

Tel	UT date (yyyy–mm–dd)	MJD	Eph	RTT (s)	PTX (kW)	δr (m)	δf (Hz)	N	Start–stop (hh:mm:ss–hh:mm:ss)	Runs	Fig. 8 key
A	2012–02–12	55969	s41	67	828	cw	0.167	None	08:27:51–08:37:55	5	
			s41			15	0.075	65535	08:42:47–10:29:47	48	1–7
			s41			15	0.075	8191	10:53:18–11:09:55	8	
A	2012–02–13	55970	s41	62	860	cw	0.182	None	08:11:06–08:23:08	6	
			s43			15	0.075	65535	08:30:34–10:53:26	54	8–14
A	2012–02–14	55971	s43	58	811	cw	0.196	None	07:59:56–08:04:43	3	
			s43			15	0.075	65535	08:06:40–10:19:45	59	15–22
A	2012–02–15	55972	s43	54	785	cw	0.213	None	07:43:02–07:47:29	3	
			s43			15	0.075	65535	08:03:01–08:09:18	4	
			s47			15	0.075	65535	08:16:38–10:09:46	60	23–29
G	2012–02–15	55972	s43	54	420	cw		None	08:55:15–09:03:27	5	
			s43			75	1.532	255	09:17:48–09:33:20	9	
			s45			37.5		255	09:46:24–11:59:24	73	
			s45			37.5		255	12:15:57–12:24:09	5	
A	2012–02–16	55973	s51	51	760	cw	0.227	None	07:34:18–07:38:30	3	
			s49			15	0.075	65535	07:40:56–07:46:52	4	
						cw		None	07:48:38–07:51:06	2	
			s49			15	0.075	65535	07:53:28–09:38:16	62	30–37
G	2012–02–16	55973	s49	51	420	cw		None	09:15:46–09:23:30	5	
			s49			75	1.532	255	09:56:39–10:02:39	4	
			s49			37.5	0.488	None	11:35:21–11:46:33	7*	
			s49			15	1.0	None	12:15:54–12:47:10	18*	43–44
			s49			15	1.0	None	13:10:01–13:28:09	11*	45
			s49			15	1.0	None	13:29:04–15:29:31	70*	46–53
A	2012–02–17	55974	s53	48	775	cw	0.244	None	07:38:00–07:41:57	3	
			s53			15	0.075	65535	07:44:36–08:48:59	40	38–42
G	2012–02–17	55974	s53	48	420	cw		None	07:05:53–07:13:10	5	
			s53			75	1.532	255	07:42:55–08:00:01	11	
			s53			37.5	0.977	None	08:16:57–12:24:19	152*	54–65
G	2012–02–18	55975	s53	47	420	cw		None	07:05:51–07:12:50	5	
			s53			75	1.532	255	07:36:04–07:50:52	10	
			s53			37.5	0.977	None	08:01:15–08:31:44	20*	66
			s53			37.5	0.977	None	08:36:51–08:45:24	6*	67
G	2012–02–19	55976	s55	46	420	cw		None	07:05:51–07:12:41	5	
			s55			75	1.532	255	07:21:55–07:36:25	10	
			s55			37.5	0.977	None	07:46:12–11:13:58	136*	68–76
			s55			37.5	0.977	None	11:44:10–13:07:06	55*	77–80
G	2012–02–20	55977	s57	46	420	cw		None	07:10:51–07:17:42	5	
			s57			37.5	0.977	None	08:12:13–09:18:53	44*	81–84
			s57			37.5	0.977	None	10:31:49–11:33:59	41*	85–87
			s57			37.5	0.977	None	12:16:08–12:19:54	3*	
G	2012–02–22	55979	s59	48	420	cw		None	09:48:25–09:55:42	5	
			s59			75	0.957	255	10:02:53–10:21:35	12	
			s59			37.5	0.977	None	10:32:51–10:35:14	2*	
			s59			37.5	0.977	None	10:36:06–10:45:02	6*	
G	2012–02–23	55980	s59	51	420	cw		None	08:33:10–08:40:53	5	
			s59			75	0.957	255	08:49:48–09:09:41	12	
			s59			75	0.977	None	09:20:46–10:55:20	55*	88–90
A	2012–08–24	56163	s72	153	721	cw		None	15:10:51–15:18:25	2	
						cw		None	15:46:51–16:31:17	9	
						150	0.954	8191	16:36:59–17:41:01	13	
A	2012–08–26	56165	s72	157	722	cw		None	15:04:24–16:20:38	15	

Note: – The first column indicates the telescope: Arecibo Planetary Radar (A) or Goldstone Solar System Radar at DSS-14 (G). MJD is the modified Julian date of the observation. Eph is the ephemeris solution number used (Section 3). RTT is the round-trip light-time to the target. PTX is the transmitter power. δr and δf are the range and Doppler resolutions, respectively, of the processed data. N is the number of bauds or the length of the pseudo-random code used. The timespan of the received data is listed by their UT start and stop times. Runs is the number of transmit-receive cycles during the timespan. An asterisk (∗) indicates chirp runs. Last column indicates the key to the image numbers shown in Fig. 8.

course of the observing run and computed the heliocentric orbit using the JPL on-site orbit determination software (OSOD). The ephemeris solution was updated each time new astrometric measurements were incorporated (Table 1). Using the best ephemeris solution at any given time minimizes smearing of the images.

At the end of our February observing campaign, we were using ephemeris solution 59. A final range measurement, obtained during the asteroid's close approach in August 2012, was incorporated to generate orbit solution 74. After the shape model was finalized, we updated the orbit to solution 76 by replacing the preliminary February astrometric measurements with more accurate shape-based estimates of the range to the center of mass (Table 2).

Table 3 lists the best fit orbital parameters (solution 76) generated using 18 range measurements and 316 optical measurements. The optical measurements span February 1977 to December 2012. However we assigned 20 arcsec uncertainties to the two precovery observations from the 1977 La Silla-DSS plates, effectively removing their contribution to the fit and reducing the optical arc to the interval 2000–2012. The 1977 observations were from a single, hour-long, trailed exposure, and appear to have been reported with a ∼45 s timing error, consistent with the measurers' cautionary note "Start time and exposure length are uncertain" (MPEC 2000-L19).

The orbit computation is reliable over a period from the year 460 to 2813. Beyond this interval either the 3σ uncertainty of the Earth

close approach time (evaluated whenever the close approach distance is less than 0.1 AU) exceeds 10 days or the 3σ uncertainty of the Earth close approach distance exceeds 0.1 AU. The current *Minimum Orbit Intersection Distance* (MOID) with respect to Earth is 0.03154 AU, making 2000 ET70 a potentially hazardous asteroid (PHA).

4. Radar scattering properties

We transmitted circularly polarized waves and used two separate channels to receive echoes having the same circular (SC) and the opposite circular (OC) polarization as that of the transmitted wave (Ostro, 1993). Reflections from a plane surface reverse the polarization of the incident waves and most of the echo power is expected in the OC polarization. Echo power in the SC polarization is due to multiple reflections or reflections from structures with wavelength-scale roughness at the surface or sub-surface. A higher ratio of SC to OC power therefore indicates a greater degree of near-surface wavelength-scale roughness or multiple scattering. It is worth noting that while a larger SC to OC ratio implies a rougher surface, there is a compositional component at well (Benner et al., 2008). This *circular polarization ratio* is often denoted by μ_C. We measured μ_C for all the Arecibo spectra shown in Fig. 1 and computed an average value of $\mu_C = 0.21 \pm 0.02$, where the uncertainty is the standard deviation of the individual estimates. Observed ratios for individual spectra deviate no more than 0.03 from the average. This ratio is lower than that for the majority of NEAs with known circular polarization ratios (Mean = 0.34 ± 0.25, Median = 0.26) (Benner et al., 2008) suggesting that 2000 ET70 has a lower than average near-surface roughness at 10 cm scales.

The average radar albedo computed for the OC CW spectra shown in Fig. 1 is 0.063 ± 0.017, where the uncertainty is the standard deviation of individual estimates. The radar albedo is the ratio of the radar cross-section to the geometric cross-sectional area of the target. The radar cross-section is the projected area of a perfectly reflective isotropic scatterer that would return the same power at the receiver as the target.

In our modeling of the shape of the asteroid (Sections 6 and 7), we used a cosine law to represent the radar scattering properties of 2000 ET70:

$$\frac{d\sigma}{dA} = R(C+1)(\cos\alpha)^{2C}. \tag{7}$$

Table 2
2000 ET70 range measurements.

Date (UTC) (yyyy–mm–dd hh:mm:ss)	Range (μs)	1-σ Uncertainty (μs)	Observatory
2012–02–12 08:50:00	67220894.76	0.5	A
2012–02–12 10:03:00	66974197.50	0.5	A
2012–02–13 09:11:00	62452848.06	0.5	A
2012–02–13 09:18:00	62298918.42	0.5	A
2012–02–14 09:28:00	58061903.74	0.5	A
2012–02–14 10:06:00	57953990.18	0.5	A
2012–02–14 10:16:00	57925824.25	0.5	A
2012–02–15 08:30:00	54319877.92	0.5	A
2012–02–15 09:20:00	54206358.81	3.0	G
2012–02–15 09:47:00	54126135.16	0.5	A
2012–02–16 08:23:00	50979848.61	0.5	A
2012–02–16 09:30:00	50840187.02	0.5	A
2012–02–17 08:05:00	48327621.88	0.5	A
2012–02–17 08:43:00	48267222.55	0.5	A
2012–02–18 07:40:00	46481930.28	2.0	G
2012–02–19 07:30:00	45481292.56	2.0	G
2012–02–20 10:10:00	45483470.81	2.0	G
2012–08–24 17:08:00	153139162.28	3.0	A

Note. This table lists shape-based estimates of the range to the asteroid COM. The first column indicates the coordinated universal time (UTC) of the measurement epoch. The second column gives the ranges expressed as the RTT to the asteroid in microseconds (μs). The third column lists the 1σ range uncertainty. The fourth column indicates the radar used to make the measurement. A stands for the Arecibo Planetary Radar and G stands for the Goldstone Solar System Radar at DSS-14.

Table 3
2000 ET70 heliocentric orbital elements (solution 76).

Element	Value	1-σ Uncertainty
Eccentricity	0.123620379	6.3×10^{-8}
Semi-major axis (AU)	0.9466347364	1.2×10^{-9}
Inclination (°)	22.3232174	1.2×10^{-6}
Longitude of ascending node (°)	331.16730395	9.8×10^{-7}
Argument of perihelion (°)	46.106698	1.1×10^{-5}
Mean anomaly (°)	84.37370818	4.2×10^{-7}

Note. All orbital elements are specified at epoch 2012 December 15.0 barycentric dynamical time (TDB) in the heliocentric ecliptic reference frame of J2000. The corresponding orbital period is $(336.41246710 \pm 5.5 \times 10^{-7})$ days.

Here σ is the radar cross section, A is the target surface area, R is the Fresnel reflectivity, C is a parameter describing the wavelength-scale roughness, and α is the incidence angle. Values of C close to 1 represent diffuse scattering, whereas larger values represent more specular scattering (Mitchell et al., 1996). For specular scattering, C is related to the wavelength-scale adirectional root-mean-square (RMS) slope S_0 and angle θ_{rms} of the surface by $S_0 = \tan(\theta_{rms}) = C^{-1/2}$.

5. Range and Doppler extents

The range extent of the object in the radar images varies between ∼600 m and ∼1700 m (Fig. 8), suggesting that the asteroid is significantly elongated. In most of the images two distinct ridges that surround a concavity are clearly visible (e.g., Fig. 8, images 8–12 and images 30–37). In images where the ridges are aligned with the Doppler axis, they span almost the entire bandwidth extent of the asteroid (e.g., Fig. 8, images 11 and 34). If the concavity is a crater then these ridges could mark its rim. At particular viewing geometries, the trailing end of the asteroid exhibits a large outcrop with a range extent of ∼250 m (e.g., Fig. 8, image 11). These features suggest that the overall surface of the asteroid is highly irregular at scales of hundreds of meters.

For a spherical object, the bandwidth (B) of the radar echo is given by:

$$B = \frac{4\pi D}{\lambda P} \cos\delta. \tag{8}$$

Here D is the diameter of the object, P is its apparent spin period, λ is the radar wavelength, and δ is the sub-radar latitude. As δ increases, B decreases. In images obtained at similar rotational phases, the bandwidth extent of the asteroid increased from February 12 to 20, indicating that our view was more equatorial towards the end of the observing campaign (Fig. 2). For example in Fig. 8, images 10, 33, and 68 are at similar rotational phases and their bandwidths (based on a 2380 MHz carrier) are ∼3.7 Hz, ∼4.9 Hz, and ∼6.3 Hz, respectively.

6. Spin vector

We used the SHAPE software (Hudson, 1993; Magri et al., 2007) to fit a shape model to the radar images and to estimate the spin vector of 2000 ET70. Since SHAPE is not particularly effective at fitting the spin axis orientation and spin period of the shape model, we carried out an extensive search for these parameters in an iterative manner. We performed two iterations each in our search for the spin axis orientation and spin period, where the result of each step provides initial conditions for the next optimization step. This approach leads to increased confidence that a global minimum is reached.

Our initial estimate of the spin period came from the time interval between repeating rotational phases of the object captured in the images. Fig. 3 shows the object at similar orientations in images taken on different days. The time interval in two of those cases is ∼72 h and in the third case is ∼45 h. This indicates that the spin period of the object is close to a common factor of the two, that is, 9 h or a sub-multiple of 9 h. Fig. 4 shows two images
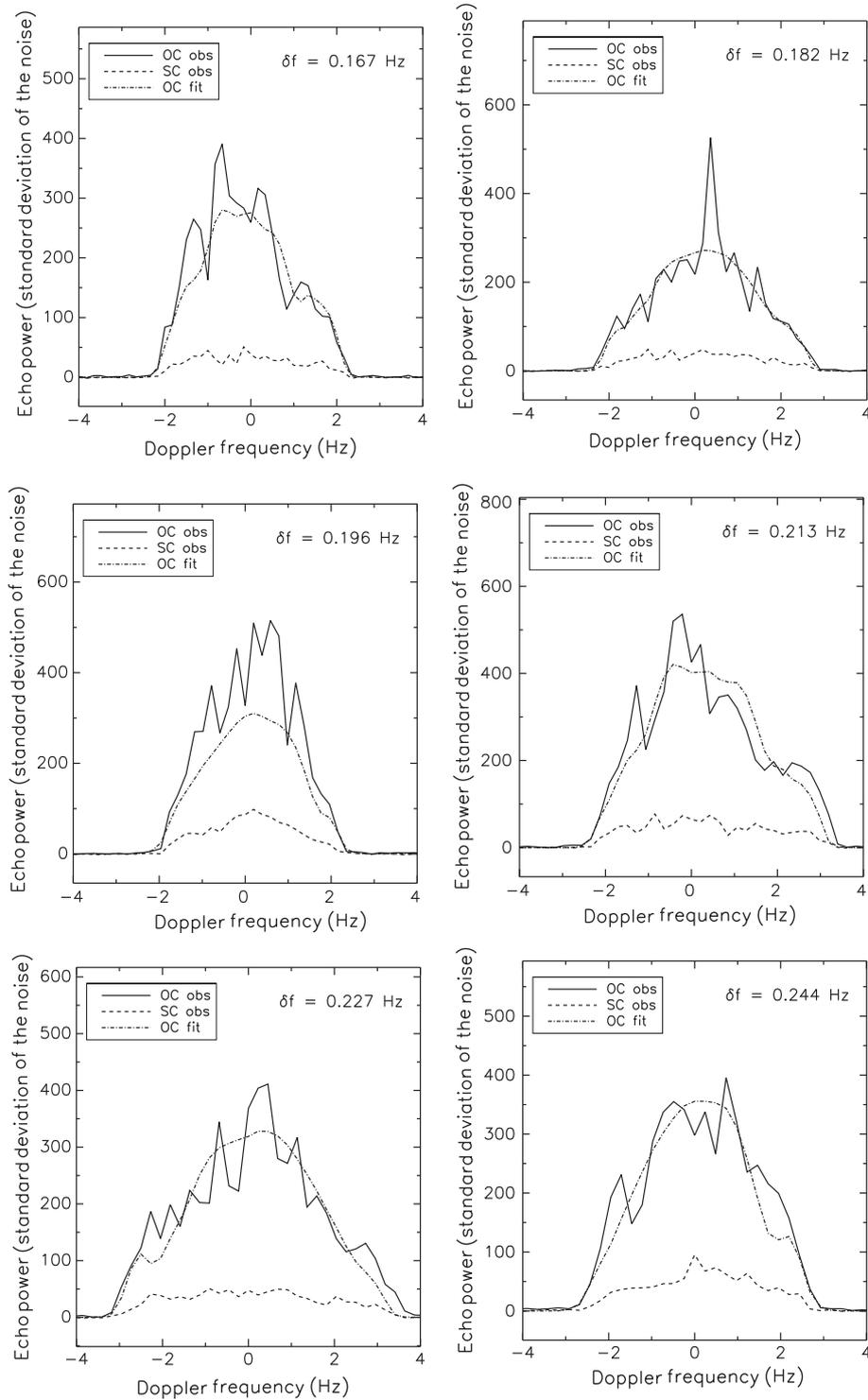
Fig. 1. Arecibo CW spectra of 2000 ET70 arranged in chronological order from left to right and top to bottom. They were obtained on February 12–17 (MJDs 55969.35, 55970.34, 55971.33, 55972.32, 55973.32, 55974.32, respectively). The frequency resolution of each spectrum is given at the top right of the corresponding panel. Each spectrum was produced by choosing a frequency resolution that allowed for the incoherent sum of 10 independent spectra, or *looks*, per run, and by summing over 3 runs, resulting in a total number of 30 looks. The solid and dashed lines are observed OC and SC spectra, respectively. The dot-dashed line shows the corresponding synthetic OC spectra generated using our shape model (Section 7). The circular polarization ratio (μ_C) values in chronological order are 0.18, 0.20, 0.24, 0.21, 0.21, and 0.24 all of which have uncertainties of 5%, where the uncertainty is computed according to Ostro et al. (1983). The OC radar albedo values in chronological order are 0.091, 0.063, 0.073, 0.056, 0.051, and 0.044 all of which have uncertainties of 25%. The reduced chi-squares of the fits to the OC spectra vary between 0.69 to 0.72.

taken 22.5 h apart and the object is not close to similar orientations in these two images, ruling out all periods that are factors of 22.5 h. Thus we are left with a period close to 3 h or 9 h. Images obtained over observing runs longer than 3 h do not show a full rotation of the asteroid, ruling out a spin period of 3 h.

Using an initially fixed spin period of 9 h, we performed an extensive search for the spin axis orientation. The search consisted of fitting shape models to the images under various assumptions for the spin axis orientation. We covered the entire celestial sphere with uniform angular separations of 15° between neighboring trial poles.

At this stage we used a subset of the images in order to decrease the computational burden. We chose images showing sharp features that repeated on different days because they provide good constraints on the spin state. Images obtained on February 12 and 15 satisfied these criteria and we used images with receive times spanning MJDs 55969.426–55969.463 and 55972.335–55972.423 for this search. We started with triaxial ellipsoid shapes and allowed the least-squares fitting procedure to adjust all three ellipsoid dimensions in order to provide the best match between model and images. We then used shapes defined by a vertex model with 500 vertices and 996 triangular facets. The fitting procedure was allowed to adjust the positions of the vertices to minimize the misfit. In all of these fits the spin axis orientation and the spin rate were held constant. Radar scattering parameters R and C described in Eq. (7) were allowed to float. We found the best shape model fit with the spin pole at ecliptic longitude (λ) = 60° and ecliptic latitude (β) = −60°.

Using the best fit spin pole from the previous step, we proceeded to estimate the spin period with greater precision. We tried spin rates in increments of 2°/day from 960°/day (P = 9 h) to 970°/day (P = 8.91 h) to fit vertex shape models with 500 vertices to the images. This time we used a more extensive dataset consisting of all images obtained from Arecibo. As in the previous step, only the radar scattering parameters and the shape parameters were allowed to float in addition to the parameter of interest. We found the best agreement between model and observations with a spin rate of 964°/day (Period = 8.963 h).

The second iteration of the spin-axis orientation search was similar to the first one except that we used a spin period of 8.963 h and used the complete dataset consisting of all the Arecibo and Goldstone images from February. The Arecibo images from August were not used because of their low SNR and resolution. This procedure was very effective in constraining the possible spin axis orientations to a small region (around λ = 79° and β = −42°) of the celestial sphere (Fig. 5). We performed a higher resolution search within this region with spin poles ranging in λ from 64° to 104° and β from −60° to −30° with step sizes of 4° in λ and 5° in β. For this step we performed triaxial ellipsoid fits followed by spherical harmonics model fits, adjusting spherical harmonic coefficients up to degree and order 10. Our best estimate of the spin axis orientation is λ = 80° and β = −50°, with 10° uncertainties. Shape models with spin axis orientations within this region have similar appearance upon visual inspection. We also attempted shape model fits with the best-fit prograde pole at λ = 232° and β = 75°. We found that we were unable to match the observed bandwidths and ruled out the prograde solution. 2000 ET70 is a retrograde spinner, just like the majority of NEAs (La Spina et al., 2004). Our adopted spin pole (λ = 80°, β = −50°) is at an angle of ~160° from the heliocentric orbit pole (λ = 241°, β = 68°).

Fig. 3. 2000 ET70 range-Doppler images showing the asteroid at similar rotational phases on different days. The images were obtained at MJDs 55970.40 and 55973.38 (~72 h apart) (top), 55971.35 and 55974.33 (~72 h apart) (center), 55969.46 and 55971.34 (~45 h apart) (bottom), suggesting a spin period of ~9 h or a sub-multiple of ~9 h. In these images radar illumination is from the top, range increases towards the bottom, Doppler frequency increases to the right, and the asteroid spin results in counter-clockwise rotation.

We used the best spherical harmonics shape model from the previous search to perform a second iteration of the spin period search. This time we fit spherical harmonics shape models using spin periods in increments of 0.001 h from 8.940 h to 8.980 h. This final step was performed in part to quantify error bars on the spin period. The reduced chi-squares of the shape models, computed according to the method described in Magri et al. (2007), are shown in Fig. 6. We visually verified the quality of the fits and adopted a spin period of 8.960 ± 0.01 h. A 0.01 h difference in spin

Fig. 4. 2000 ET70 images obtained at MJDs 55970.40 and 55971.34, or 22.5 h apart. The asteroid is not close to similar rotational phases in these images, ruling out spin periods that are sub-multiples of ~22.5 h. A ~4.5-h spin period is therefore ruled out, leaving ~9 h as the only plausible value.

Fig. 2. Sub-radar point (SRP) latitude during the primary observing period. Solid and dashed lines show SRP latitude for the prograde and retrograde spin vectors, respectively (Section 6).
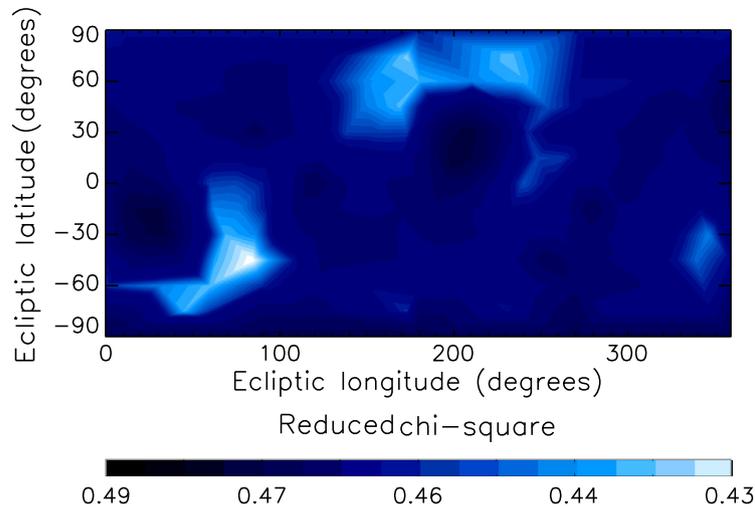
Fig. 5. Contour plot showing goodness of fit (reduced chi-square) of shape model fits under various assumptions for the ecliptic longitude (λ) and ecliptic latitude (β) of the spin axis. The spin period was fixed at 8.963 h for the fits. We adopted a best fit spin axis orientation of $\lambda = 80°$ and $\beta = -50°$ with a 10° uncertainty.

period amounts to a ~13° offset in rotational phase over the primary observing window which is detectable.

7. Shape model

As a starting point for our final shape modeling efforts we used the results of the spin state determination (Section 6), specifically the best-fit spherical harmonics shape model with a spin period of 8.960 h and a spin pole at $\lambda = 80°$ and $\beta = -50°$. We proceeded to fit all the radar images obtained in February and OC CW spectra from Fig. 1 with a vertex model having 2000 vertices and 3996 facets. The number of vertices is based on experience and the desire to reproduce detectable features without over-interpretation. At this step the vertex locations and the radar scattering parameters were fit for, but the spin vector was held fixed. Observed images were summed to improve their SNR. At Arecibo, 8 images were typically combined. At Goldstone, 14, 9, 13, 13, 14, 12, 6, and 12 images were typically combined on February 15, 16, 17, 18, 19, 20, 22, and 23, respectively. We cropped the images so that sufficient sky background remained for the computation of noise statistics, but the optimization procedure is robust against the amount of sky background. We minimized an objective function that consists of the sum of squares of residuals between model and actual images, plus a number of weighted penalty functions designed to favor models with uniform density, principal axis rotation, and a reasonably smooth surface (Hudson, 1993; Magri et al., 2007). The choice of weights in the penalty function is subjective, so the shape model solution is not unique. We tried to restrict the weights to the minimum value at which the penalty functions were effective. The minimization procedure with our choice of penalty functions produced a detailed shape model for 2000 ET70 (Fig. 7 and Table 4). The agreement between model and data is generally excellent but minor disagreements are observed (Figs. 8 and 1). The overall shape is roughly a triaxial ellipsoid with extents along the principal axes of ~2.61 km, ~2.22 km, and ~2.04 km, which are roughly the same as the *dynamically equivalent equal volume ellipsoid* (DEEVE) dimensions listed in Table 4.

The region around the north pole has two ridges that are 1–1.5 km in length and almost 100 m higher than their surroundings. These ridges enclose a concavity that seems more asymmetric than most impact craters. Along the negative *x*-axis a large protrusion is visible. Such a feature could arise if the asteroid were made up of multiple large components resting on each other.

NEAs in this size range for which radar shape models exist commonly exhibit irregular features such as concavities and ridges. A few examples include Golevka (Hudson et al., 2000), 1992 SK (Busch et al., 2006), and 1998 WT24 (Busch et al., 2008). The
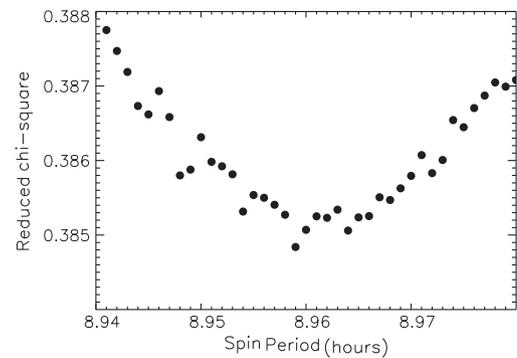
Fig. 6. Goodness of fit (reduced chi-square) of degree-and-order 10 spherical harmonics shape models of 2000 ET70 as a function of assumed spin period. The spin pole was fixed at $\lambda = 80°$ and $\beta = -50°$ for the fits. We adopted a best fit spin period of 8.960 ± 0.01 h.

concavities observed on these NEAs cannot be adequately captured by convex-only shape modeling techniques.

For this shape model, the best fit values for the radar scattering parameters, R and C, were 1.9 and 1.4, respectively (Section 4). This value of C indicates that 2000 ET70 is a diffuse scatterer, simlar to other NEAs such as Geographos (Hudson and Ostro, 1999), Golevka (Hudson et al., 2000), and 1998 ML14 (Ostro et al., 2001). NEAs are generally expected to be diffuse scatterers at radar wavelengths because of their small sizes and rough surfaces. Attempts to fit the echoes with a two-component scattering law (diffuse plus specular) did not yield significantly better results.

8. Gravitational environment

We used our best-fit shape model and a uniform density assumption of 2000 kg m^{-3}, a reasonable density for rubble-pile NEAs, (e.g., Ostro et al., 2006), to compute the gravity field at the surface of the asteroid (Werner and Scheeres, 1997). The acceleration on the surface is the sum of the gravitational acceleration due to the asteroid's mass and the centrifugal acceleration due to the asteroid's spin. An acceleration vector was computed at the center of each facet. Fig. 9 shows the variation of the magnitude of this acceleration over the surface of the asteroid. The acceleration on the surface varies between 0.54 mm s^{-2} to 0.64 mm s^{-2}, which is four orders of magnitude smaller than that experienced on Earth and two orders of magnitude smaller than that on Vesta. Centrifu-
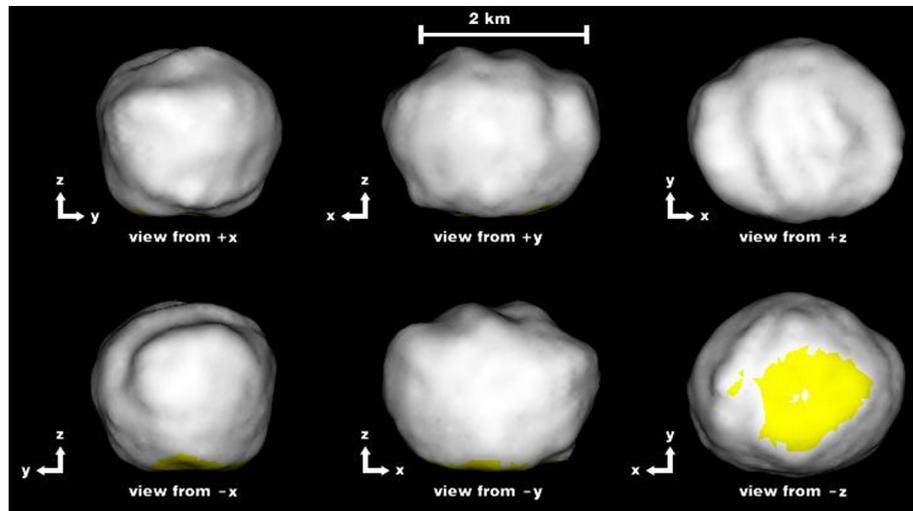
Fig. 7. Best-fit vertex shape model of 2000 ET70 as seen along the three principal axes *x*, *y*, and *z*. For principal axis rotation the spin axis is aligned with the *z* axis. Yellow regions at the south pole have radar incidence angles >60° and hence are not well constrained. The shape model has 2000 vertices and 3996 triangular facets giving an effective surface resolution of ∼100 m. (For interpretation of the references to color in this figure legend, the reader is referred to the web version of this article.)

gal acceleration makes a significant contribution to the total acceleration and varies from zero at the poles to ∼0.049 mm s^{-2} (about 10% of the total acceleration) on the most protruding regions of the equator. For comparison, on Earth, centrifugal acceleration contributes less than 0.5% to the total acceleration at the equator.

Fig. 10 shows the gravitational slope variation over the asteroid's surface. The gravitational slope is the angle that the local gravitational acceleration vector makes with the inward pointing surface-normal vector. The average slope is 9.5°. Less than 1% of the surface has slopes greater than 30°, the approximate angle of repose of sand, indicating a relaxed surface. Slopes on the sides of the ridges near the north pole reach up to ∼33°, and the sides facing the north pole are steeper than the opposite sides. As a result of the high slopes, along-the-surface accelerations are a substantial fraction of the total acceleration, reaching values as high as 0.34 mm s^{-2}. One might expect mass wasting to result from this gravitational environment: the sides of the ridges may have competent rocks exposed at the surface, and the valley between the two ridges may be overlain by a pond of accumulated regolith. A similar mass wasting process is hypothesized to have occurred on Eros (Zuber et al., 2000). The accumulation of fine-grained regolith could lower the wavelength-scale surface roughness locally and perhaps explain the lower values of μ_C observed at higher SRP latitudes (Fig. 1). A similar trend in μ_C was observed in the Goldstone CW spectra.

9. Discussion

Whiteley (2001) and Williams (2012) estimated 2000 ET70's absolute magnitude (*H*) to be near 18.2. The geometric albedo (p_V) of an asteroid is related to its effective diameter (*D*) and its *H* value by (Pravec and Harris, 2007, and references therein):

$$p_V = \left[\frac{1329 \text{ km} \times 10^{-0.2H}}{D} \right]^2. \tag{9}$$

Using Whiteley's (2001) *H* = 18.2, the above equation yields p_V = 0.018 ± 0.002 for an asteroid with an effective diameter of 2.26 km ± 5% (Fig. 11). This uncertainty on p_V is due to the diameter uncertainty only. A geometric albedo near 2% is extremely low compared to the albedos of other NEAs (Thomas et al., 2011; Stuart et al., 2004). More common values of p_V would require lower values of the absolute magnitude (e.g., p_V = 0.04 requires *H* = 17.5). The range of possible *H* and p_V values that are consistent with the radar

Table 4
2000 ET70 shape model parameters.

Parameters		Value
Extents along principal axes (km)	*x*	2.61 ± 5%
	y	2.22 ± 5%
	z	2.04 ± 5%
Surface area (km^2)		16.7 ± 10%
Volume (km^3)		6.07 ± 15%
Moment of inertia ratios	*A/C*	0.800 ± 10%
	B/C	0.956 ± 10%
Equivalent diameter (km)		2.26 ± 5%
DEEVE extents (km)	*x*	2.56 ± 5%
	y	2.19 ± 5%
	z	2.07 ± 5%
Spin pole (λ, β) (°)		(80, −50) ± 10
Sidereal spin period (h)		8.96 ± 0.01

Note. The shape model consists of 2000 vertices and 3996 triangular facets, corresponding to an effective surface resolution of ∼100 m. The moment of inertia ratios were calculated assuming homogeneous density. Here *A*, *B*, and *C* are the principal moments of inertia, such that *A* < *B* < *C*. Equivalent diameter is the diameter of a sphere having the same volume as that of the shape model. A *dynamically equivalent equal volume ellipsoid* (DEEVE) is an ellipsoid with uniform density having the same volume and moment of inertia ratios as the shape model.

size estimates is shown in Fig. 11. We conclude that 2000 ET70 has either an extremely low albedo or unusual phase function.

Alvarez et al. (2012) observed the asteroid between February 19 and 24, when the view was close to the equator, and reported a lightcurve amplitude of 0.60 ± 0.07 mag. If the asteroid was approximated by a triaxial ellipsoid with uniform albedo, this amplitude would suggest an elongation (ratio of equatorial axes) approximately between 1.28 and 1.36. Our shape model indicates that this ratio is ∼1.18, suggesting that either the ellipsoid approximation is poor, the lightcurve amplitude is on the lower end of the range above, shadowing due to the terrain is playing an important role, there are albedo variations over the surface of the asteroid, or a combination of these factors.

Alvarez et al. (2012) also report a lightcurve period of 8.947 ± 0.001 h. Their reported period is a function of the intrinsic spin state of the asteroid and of the relative motion between the asteroid, the observer, and the Sun. Therefore, it is close to but not exactly equivalent to the *synodic period*, which combines the (fixed) intrinsic rotation and the (variable) apparent rotation due to sky motion, but is independent of the position of the Sun. If we assume that the reported lightcurve period is equivalent to the synodic period, we can compute the corresponding sidereal periods. This
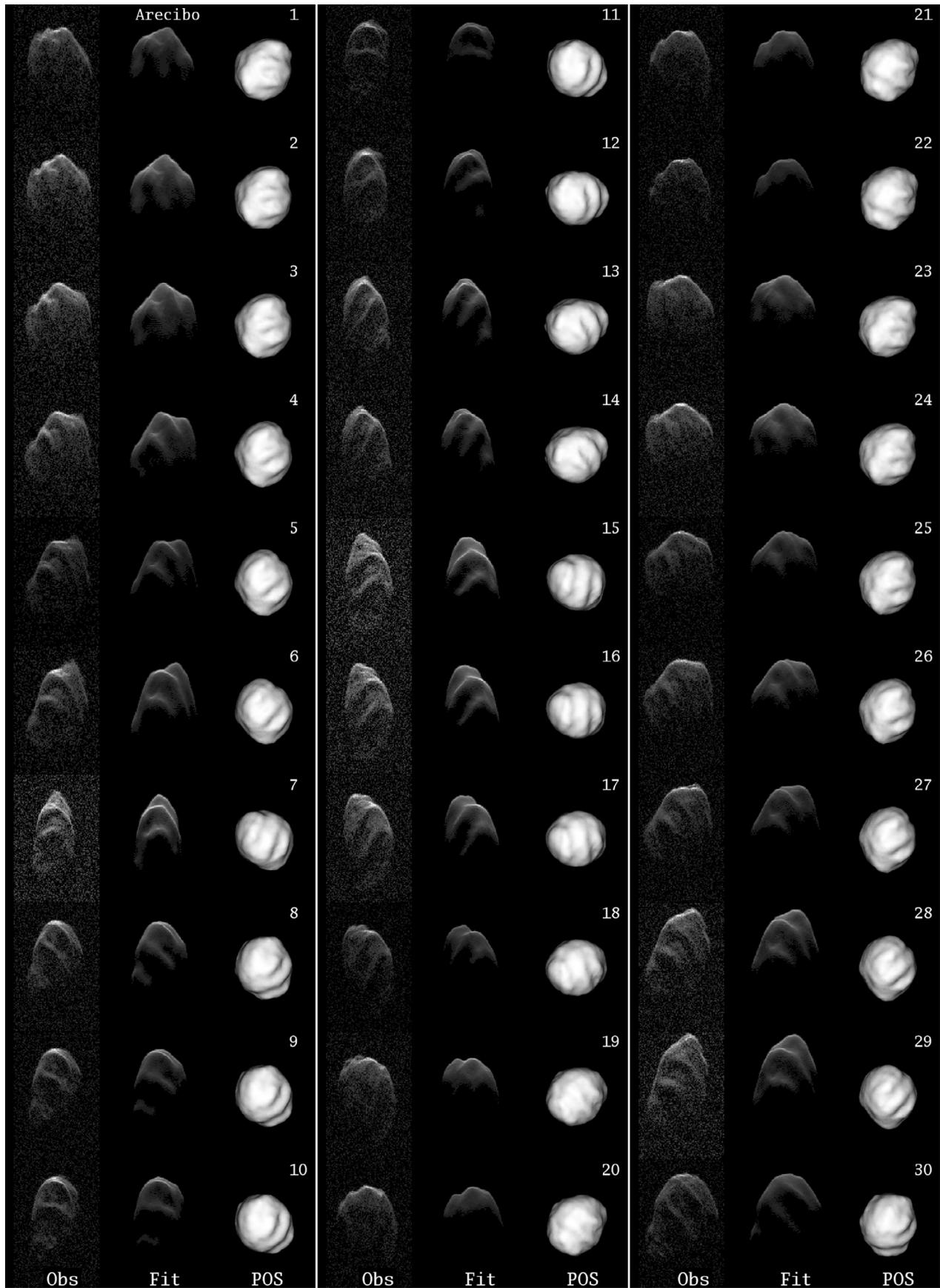
Fig. 8. Comparison between radar range-Doppler images, corresponding synthetic radar images generated using our best-fit shape model, and plane-of-sky (POS) projections of the shape model. Range-Doppler images are oriented such that radar illumination is from the top, range increases towards the bottom, Doppler frequency increases to the right, and the asteroid spin results in counter-clockwise rotation. The POS projections are oriented north-up and east-left. Time increases from top to bottom within each panel and from left to right. The range and frequency resolutions of the images are given in Table 1. The reduced chi-square of the fit to the images is 0.27.
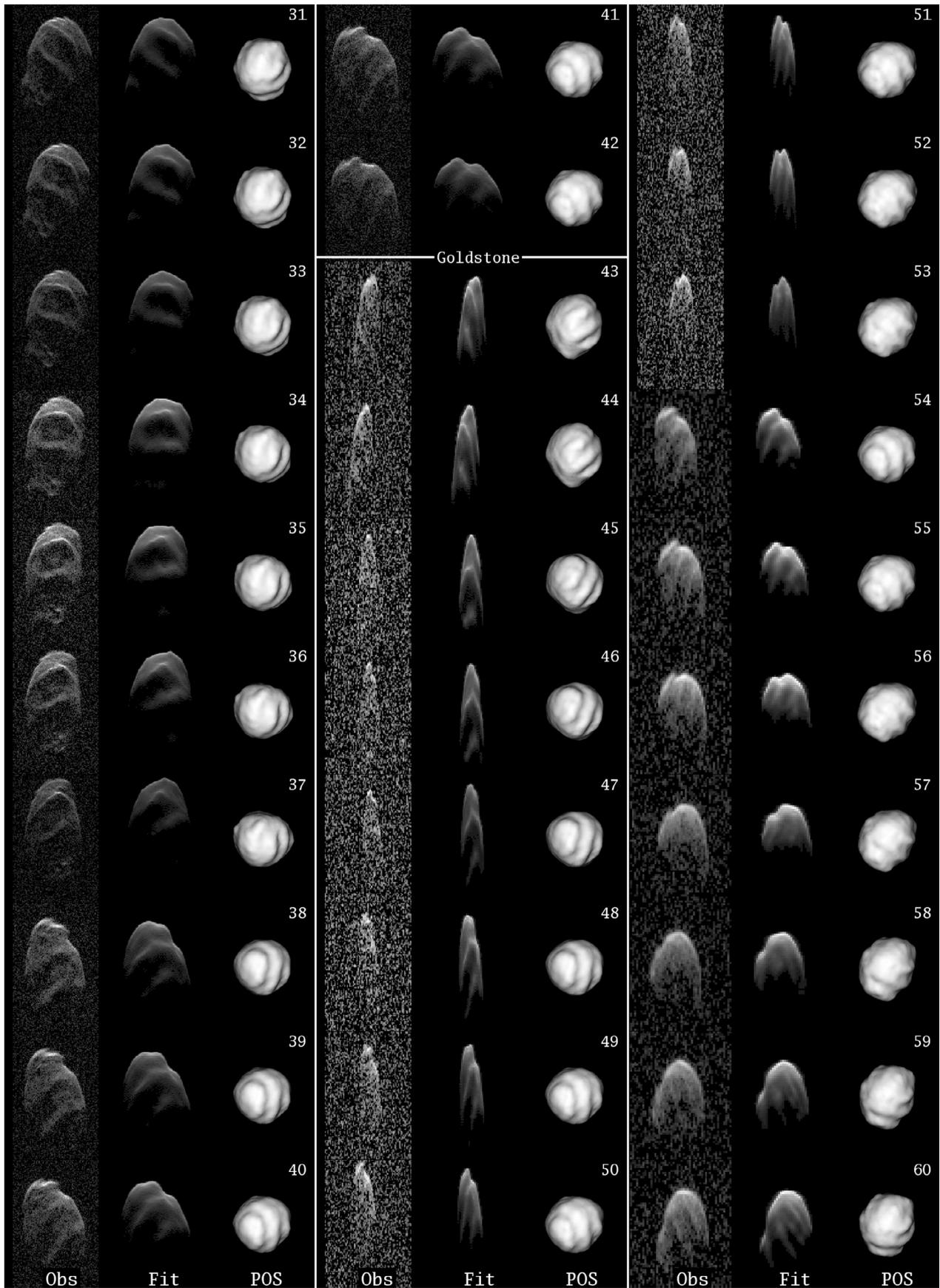
Fig. 8 (*continued*)
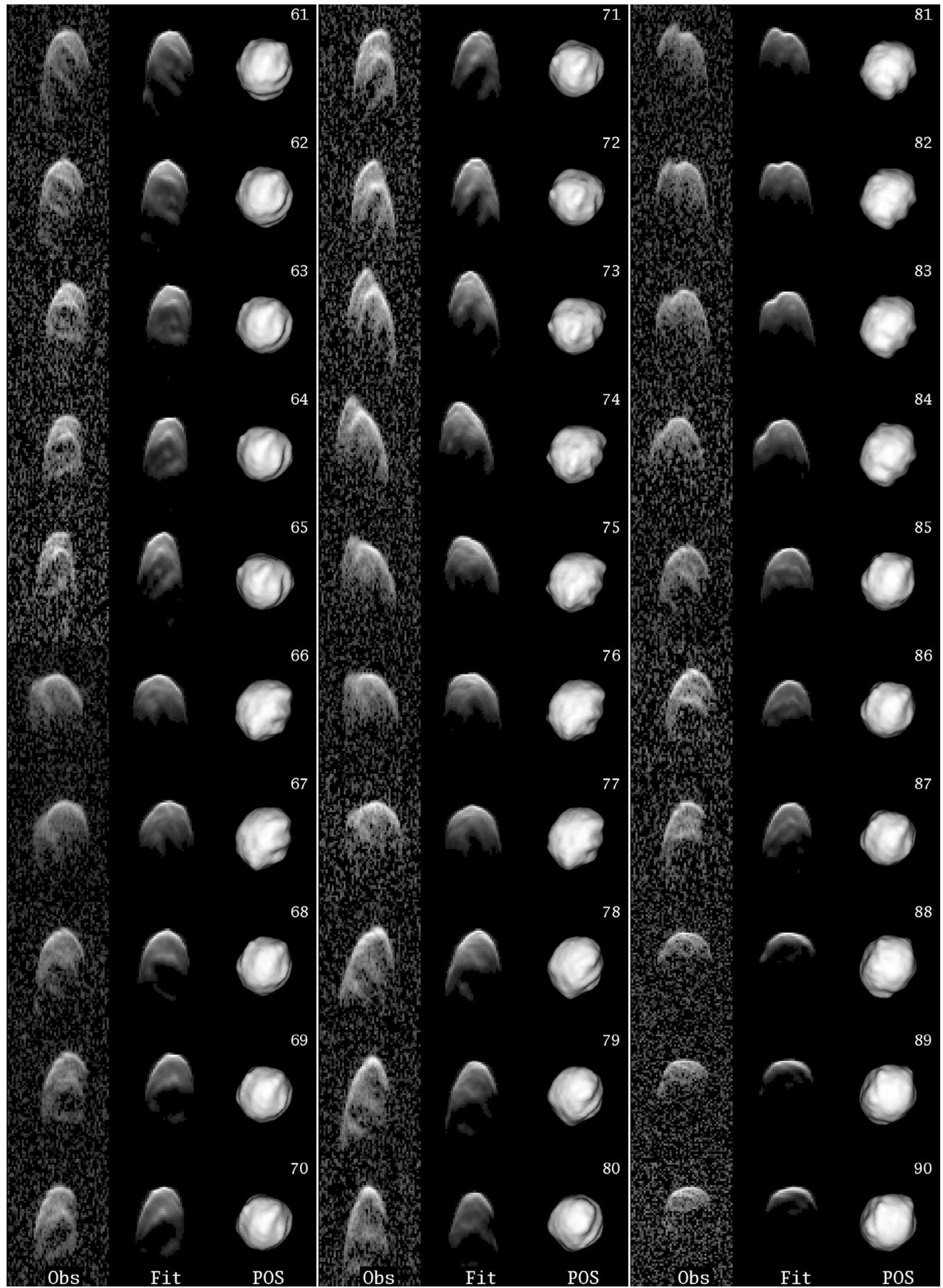
Fig. 8 (*continued*)
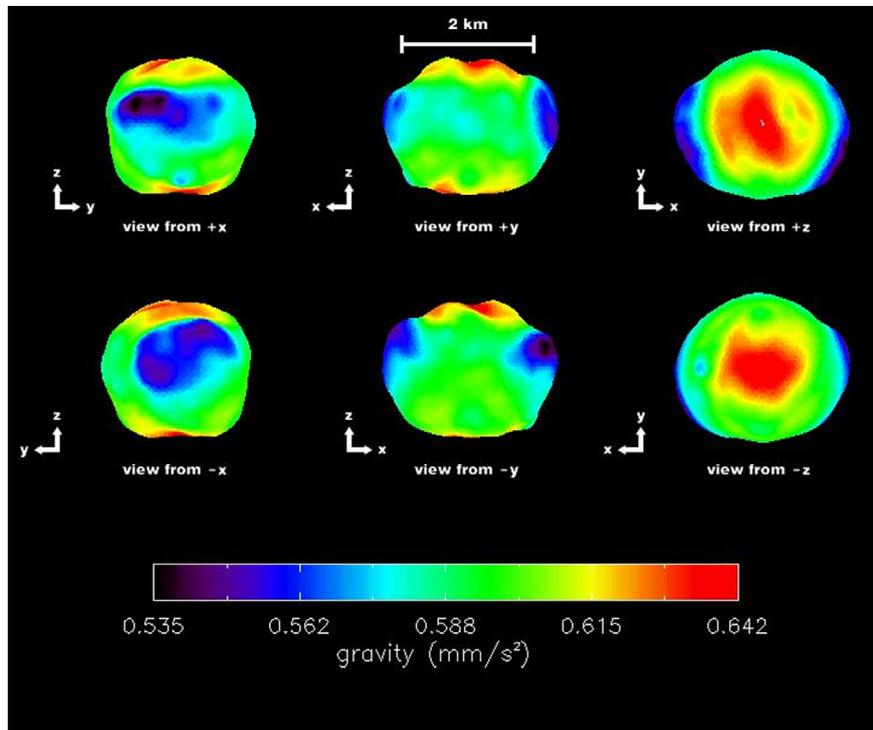
Fig. 9. This figure shows the magnitude of the vector sum of acceleration due to gravity and centrifugal acceleration computed at the center of each facet of the shape model. We assumed a uniform density of 2000 kg m^{-3} and used our measured spin period value of 8.96 h. Centrifugal acceleration makes a significant contribution to the total acceleration; at the most protruding regions of the equator it accounts for about 10%.
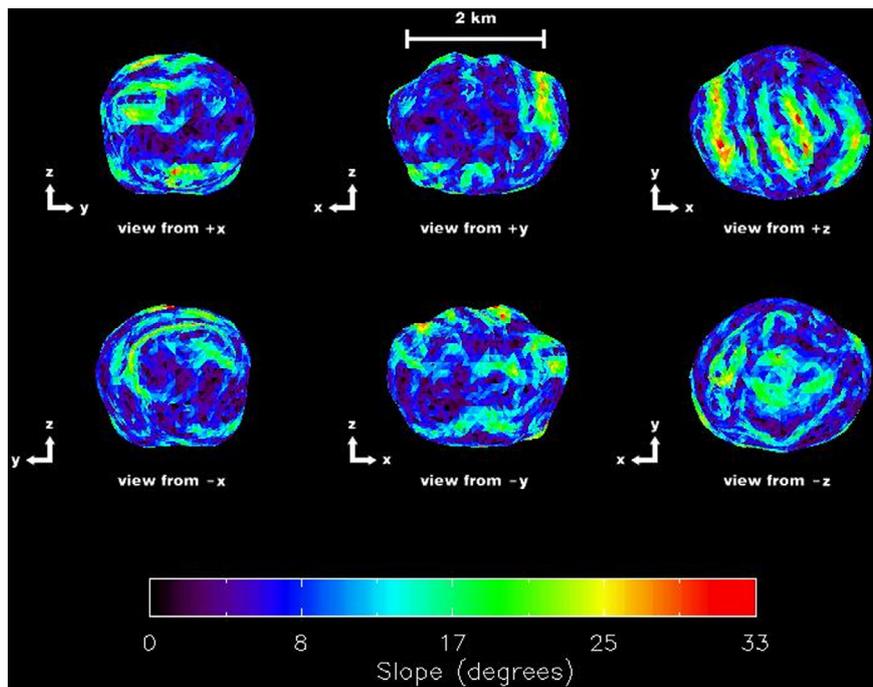
Fig. 10. This figure shows the gravitational slopes computed at the center of each facet of the shape model. The gravitational slope is the angle that the local gravitational acceleration vector makes with the inward pointing surface-normal vector. We assumed a uniform density of 2000 kg m^{-3} and used our measured spin period value of 8.96 h. Sides of the ridges near the north pole have slopes exceeding 30°, the approximate angle of repose of sand.

transformation depends on the spin axis orientation. In the absence of information about the spin axis orientation, a synodic period of 8.947 maps into sidereal periods between 8.902 h and 8.992 h, i.e., a range that is about 100 times larger than the precision reported for the lightcurve period. This range includes the sidereal period that we derived from the shape modeling process (8.960 ± 0.01 h). If we use our value and our best-fit spin axis orientation we can evaluate

corresponding synodic periods at various epochs. On Feb 19.0, the nominal synodic period was 8.937 h, whereas on Feb 25.0, the nominal synodic period was 8.943 h. These synodic periods are close to the reported lightcurve period, but cannot be directly compared to it as they measure slightly different phenomena.

Arecibo and Goldstone radar observations of 2000 ET70 allowed us to provide a detailed characterization of a potentially hazardous
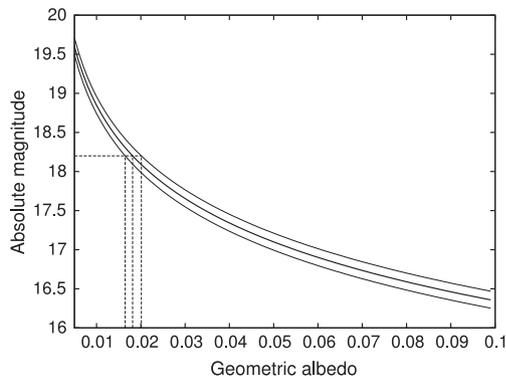
Fig. 11. Absolute magnitude vs. geometric albedo for an effective diameter of 2.26 km (dark line) and a diameter uncertainty of 5% (light lines). The horizontal dashed line corresponds to the absolute magnitude (H = 18.2) reported by Whiteley (2001), and the vertical dashed lines indicate the corresponding geometric albedos. These albedo values are unusually low, suggesting an extraordinarily dark object or an object having an unusual phase function.

asteroid, including its size, shape, spin state, scattering properties, and gravitational environment. These techniques are applicable to a substantial fraction of known NEAs that make close approaches to Earth within ∼0.1 AU. Radar-based physical properties for this and other asteroids are available at http://radarastronomy.org.

References

Alvarez, E.M. et al., 2012. Period determination for NEA (162421) 2000 ET70. Minor Planet Bull. 39, 170.

Benner, L.A.M., Ostro, S.J., Nolan, M.C., Margot, J.L., Giorgini, J.D., Hudson, R.S., Jurgens, R.F., Slade, M.A., Howell, E.S., Campbell, D.B., Yeomans, D.K., 2002. Radar observations of Asteroid 1999 JM8. Meteorit. Planet. Sci. 37, 779–792.

Benner, L.A.M., Nolan, M.C., Ostro, S.J., Giorgini, J.D., Pray, D.P., Harris, A.W., Magri, C., Margot, J.L., 2006. Near-Earth Asteroid 2005 CR37: Radar images and photometry of a candidate contact binary. Icarus 182, 474–481.

Benner, L.A.M., Ostro, S.J., Magri, C., Nolan, M.C., Howell, E.S., Giorgini, J.D., Jurgens, R.F., Margot, J.L., Taylor, P.A., Busch, M.W., Shepard, M.K., 2008. Near-Earth asteroid surface roughness depends on compositional class. Icarus 198, 294–304. http://dx.doi.org/10.1016/j.icarus.2008.06.010.

Brozovic, M., Benner, L.A.M., Magri, C., Ostro, S.J., Scheeres, D.J., Giorgini, J.D., Nolan, M.C., Margot, J.L., Jurgens, R.F., Rose, R., 2010. Radar observations and a physical model of contact binary Asteroid 4486 Mithra. Icarus 208, 207–220.

Brozović, M., Benner, L.A.M., Taylor, P.A., Nolan, M.C., Howell, E.S., Magri, C., Scheeres, D.J., Giorgini, J.D., Pollock, J.T., Pravec, P., Galád, A., Fang, J., Margot, J.L., Busch, M.W., Shepard, M.K., Reichart, D.E., Ivarsen, K.M., Haislip, J.B., Lacluyze, A.P., Jao, J., Slade, M.A., Lawrence, K.J., Hicks, M.D., 2011. Radar and optical observations and physical modeling of triple near-Earth Asteroid (136617) 1994 CC. Icarus 216, 241–256.

Busch, M.W., Ostro, S.J., Benner, L.A.M., Giorgini, J.D., Jurgens, R.F., Rose, R., Magri, C., Pravec, P., Scheeres, D.J., Broschart, S.B., 2006. Radar and optical observations and physical modeling of near-Earth asteroid 10115 (1992 SK). Icarus 181, 145–155. http://dx.doi.org/10.1016/j.icarus.2005.10.024.

Busch, M.W., Benner, L.A.M., Ostro, S.J., Giorgini, J.D., Jurgens, R.F., Rose, R., Scheeres, D.J., Magri, C., Margot, J.-L., Nolan, M.C., Hine, A.A., 2008. Physical properties of near-Earth Asteroid (33342) 1998 WT24. Icarus 195, 614–621. http://dx.doi.org/10.1016/j.icarus.2008.01.020.

Chesley, S.R. et al., 2003. Direct detection of the Yarkovsky effect by radar ranging to Asteroid 6489 Golevka. Science 302, 1739–1742.

DeMeo, F.E., Binzel, R.P., Slivan, S.M., Bus, S.J., 2009. An extension of the Bus asteroid taxonomy into the near-infrared. Icarus 202, 160–180. http://dx.doi.org/10.1016/j.icarus.2009.02.005.

Fang, J., Margot, J.L., 2012. Near-Earth binaries and triples: Origin and evolution of spin–orbital properties. Astron. J. 143, 24. http://dx.doi.org/10.1088/0004-6256/143/1/24.

Fang, J., Margot, J.L., Brozovic, M., Nolan, M.C., Benner, L.A.M., Taylor, P.A., 2011. Orbits of near-Earth Asteroid Triples 2001 SN263 and 1994 CC: Properties, origin, and evolution. Astron. J. 141, 154–168.

Hudson, S., 1993. Three-dimensional reconstruction of asteroids from radar observations. Remote Sens. Rev. 8, 195–203.

Hudson, R.S., Ostro, S.J., 1994. Shape of Asteroid 4769 Castalia (1989 PB) from inversion of radar images. Science 263, 940–943.

Hudson, R.S., Ostro, S.J., 1999. Physical model of Asteroid 1620 Geographos from radar and optical data. Icarus 140, 369–378. http://dx.doi.org/10.1006/icar.1999.6142.

Hudson, R.S., Ostro, S.J., Jurgens, R.F., Rosema, K.D., Giorgini, J.D., Winkler, R., Rose, R., Choate, D., Cormier, R.A., Franck, C.R., Frye, R., Howard, D., Kelley, D., Littlefair, R., Slade, M.A., Benner, L.A.M., Thomas, M.L., Mitchell, D.L., Chodas, P.W., Yeomans, D.K., Scheeres, D.J., Palmer, P., Zaitsev, A., Koyama, Y., Nakamura, A., Harris, A.W., Meshkov, M.N., 2000. Radar observations and physical model of Asteroid 6489 Golevka. Icarus 148, 37–51. http://dx.doi.org/10.1006/icar.2000.6483.

La Spina, A., Paolicchi, P., Kryszczyńska, A., Pravec, P., 2004. Retrograde spins of near-Earth asteroids from the Yarkovsky effect. Nature 428, 400–401. http://dx.doi.org/10.1038/nature02411.

Lowry, S.C. et al., 2007. Direct detection of the asteroidal YORP effect. Science 316, 272–274.

Magri, C., Ostro, S.J., Scheeres, D.J., Nolan, M.C., Giorgini, J.D., Benner, L.A.M., Margot, J.L., 2007. Radar observations and a physical model of Asteroid 1580 Betulia. Icarus 186, 152–177. http://dx.doi.org/10.1016/j.icarus.2006.08.004.

Margot, J.L., 2001. Planetary Radar Astronomy with Linear FM (chirp) Waveforms. Arecibo Technical and Operations Memo Series 2001–09. Arecibo Observatory. http://www.naic.edu/~astro/aotms/misc/chirp.pdf.

Margot, J.L. et al., 2002. Binary asteroids in the near-Earth object population. Science 296, 1445–1448. http://dx.doi.org/10.1126/science.1072094.

Mitchell, D.L., Ostro, S.J., Hudson, R.S., Rosema, K.D., Campbell, D.B., Velez, R., Chandler, J.F., Shapiro, I.I., Giorgini, J.D., Yeomans, D.K., 1996. Radar observations of Asteroids 1 Ceres, 2 Pallas, and 4 Vesta. Icarus 124, 113–133. http://dx.doi.org/10.1006/icar.1996.0193.

Nolan, M.C., Howell, E.S., Becker, T.M., Magri, C., Giorgini, J.D., Margot, J.L., 2008. Arecibo radar observations of 2001 SN263: A near-Earth triple asteroid system. Bull. Am. Astron. Soc. 40, 432.

Nugent, C.R., Margot, J.L., Chesley, S.R., Vokrouhlický, D., 2012. Detection of semi-major axis drifts in 54 near-Earth asteroids: New measurements of the Yarkovsky effect. Astron. J. 144, 60, arXiv1204.5990.

Ostro, S.J., 1993. Planetary radar astronomy. Rev. Mod. Phys. 65, 1235–1279. http://dx.doi.org/10.1103/RevModPhys.65.1235.

Ostro, S.J., Campbell, D.B., Shapiro, I.I., 1983. Radar observations of Asteroid 1685 Toro. Astron. J. 88, 565–576. http://dx.doi.org/10.1086/113345.

Ostro, S.J. et al., 1995. Radar images of Asteroid 4179 Toutatis. Science 270, 80–83. http://dx.doi.org/10.1126/science.270.5233.80.

Ostro, S.J. et al., 2001. Radar observations of Asteroid 1998 ML14. Meteorit. Planet. Sci. 36, 1225–1236. http://dx.doi.org/10.1111/j.1945-5100.2001.tb01956.x.

Ostro, S.J. et al., 2006. Radar imaging of binary near-Earth Asteroid (66391) 1999 KW4. Science 314, 1276–1280. http://dx.doi.org/10.1126/science.1133622.

Peebles, P.Z., 2007. Radar Principles. Wiley India Pvt. Limited, ISBN 9788126515271. <http://books.google.com/books?id=rnX21aAMKCIC>.

Pravec, P., Harris, A.W., 2007. Binary asteroid population. 1. Angular momentum content. Icarus 190, 250–259. http://dx.doi.org/10.1016/j.icarus.2007.02.023.

Scheeres, D.J. et al., 2006. Dynamical configuration of binary near-Earth Asteroid (66391) 1999 KW4. Science 314, 1280–1283. http://dx.doi.org/10.1126/science.1133599.

Shepard, M.K., Margot, J.L., Magri, C., Nolan, M.C., Schlieder, J., Estes, B., Bus, S.J., Volquardsen, E.L., Rivkin, A.S., Benner, L.A.M., Giorgini, J.D., Ostro, S.J., Busch, M.W., 2006. Radar and infrared observations of binary near-Earth Asteroid 2002 CE26. Icarus 184, 198–210. http://dx.doi.org/10.1016/j.icarus.2006.04.019.

Stuart, J.S., Binzel, R.P., population, Bias-corrected, distribution, size, 2004. and impact hazard for the near-Earth objects. Icarus 170, 295–311. http://dx.doi.org/10.1016/j.icarus.2004.03.018.

Taylor, P.A., Margot, J.L., 2011. Binary asteroid systems: Tidal end states and estimates of material properties. Icarus 212, 661–676.

Taylor, P.A. et al., 2007. Spin rate of Asteroid (54509) 2000 PH5 increasing due to the YORP effect. Science 316, 274. http://dx.doi.org/10.1126/science.1139038.

Tholen, D.J., 1984. Asteroid Taxonomy from Cluster Analysis of Photometry. Ph.D. Thesis, Arizona Univ., Tucson.

Thomas, C.A. et al., 2011. ExploreNEOs. V. Average albedo by taxonomic complex in the near-Earth asteroid population. Astron. J. 142, 85. http://dx.doi.org/10.1088/0004-6256/142/3/85.

Werner, R.A., Scheeres, D.J., 1997. Exterior gravitation of a polyhedron derived and compared with harmonic and mascon gravitation representations of Asteroid 4769 Castalia. Celest. Mech. Dynam. Astron. 65, 313–344.

Whiteley Jr., R.J., 2001. A Compositional and Dynamical Survey of the Near-Earth Asteroids. PhD Thesis, University of Hawai'i at Manoa.

Williams, G.V., 2012. Minor Planet Astrophotometry. Ph.D. Thesis, Smithsonian Astrophysical Observatory. gwilliams@cfa.harvard.edu.

Zuber, M.T. et al., 2000. The shape of 433 Eros from the NEAR-Shoemaker laser range-finder. Science 289, 2097–2101. http://dx.doi.org/10.1126/science.289.5487.2097.